

A Photoacoustic Technique for Depth-Resolved In Situ Monitoring of Biofilms

T. SCHMID,[†] U. PANNE,[†] C. HAISCH,[†]
M. HAUSNER,[‡] AND R. NIESSNER*[†]

Institute of Hydrochemistry, Technical University of Munich, Marchioninstr. 17, 81377 Munich, Germany, and Institute of Water Quality Control and Waste Management, Am Coulombwall, 85748 Garching, Germany

Biofilms occur in natural and engineered water systems. Biofouling in technical processes lowers the water quality and increases the frictional resistance in tubes. In wastewater treatment plants, biofilms are used for removal of organic and inorganic pollutants. For improvement of antifouling strategies and for process optimization in wastewater treatment plants, an analytical technique for on-line monitoring of biofilms is needed. In this article, a new setup for in situ monitoring of biofilms by photoacoustic spectroscopy is presented. To produce a biofilm, a mixture of microorganisms was grown in a nutrient solution inside a tube reactor. The content of the tube reactor was pumped through a flow channel, and biofilms were generated at the inner surfaces. Three photoacoustic sensor heads were integrated at different positions into the base plate of the flow channel. By photoacoustic spectroscopy, growth, thickness, and detachment of biofilms can be monitored on-line and nondestructively. Experiments presented in this article showed that the flow conditions influence the structure and thickness of biofilms. By changing the pH value, electrostatic interactions inside the biofilm matrix were influenced, and the subsequent detachment processes were observed on-line. The interaction of iron(III) oxide particles with biofilms led to particle adsorption on the outer and inner surfaces of the biofilm. Afterwards, biofilm flocs were sloughed off from the base biofilm.

Introduction

Biofilms are aggregates of microorganisms that occur at aqueous interfaces. The microbial cells are enclosed in a gel matrix formed by extracellular polymer substances (EPS) (1). The EPS consist of polysaccharides, proteins, and other biopolymers that are produced by the microorganisms themselves. Additionally, EPS can contain adsorbed macromolecules from other origins (2–4). The biofilm mass is predominantly water (85–95% wet weight), bacteria (10^9 – 10^{11} cells/mL), and EPS (1–2% wet weight) (5, 6). Despite the small EPS content, most of the physical and physicochemical properties of biofilms such as water binding, sorption of dissolved substances and particles, and mechanical stability of the biofilm are caused by the EPS (7–10).

* Corresponding author: phone ++49 89 7095 7980, fax ++49 89 7095 7999, e-mail reinhard.niessner@ch.tum.de.

[†] Institute of Hydrochemistry.

[‡] Institute of Water Quality Control and Waste Management.

Biofilms attached to solid surfaces are found in natural and engineered water systems. The unwanted deposition of biofilms in technical processes is termed biofouling. Biofouling can decrease, for example, the heat-transfer efficiency in heat exchangers and increase the pressure difference in membrane processes. Further, biofilm growth on the surface of tubes increases the frictional resistance and reduces the water quality (11). Despite these negative effects, biofilms can be used as well in beneficial applications. In biological wastewater treatment plants, immobilized microorganisms are used for degradation of organic and inorganic pollutants.

Relevant parameters that have to be monitored for optimization of degradation processes or antifouling strategies are growth, detachment, and thickness of the biofilm. Here, a new setup is presented for in situ monitoring of biofilms by photoacoustic spectroscopy (PAS). Photoacoustic spectroscopy has been extensively used for nondestructive investigations in chemical, biological, and environmental studies (12). In this study, important changes in the biofilm due to changes in pH value, flow conditions, particulates, etc., were detected for the first time in a depth-resolved fashion.

Experimental Section

Biofilm Reactor System and Biofilm Growth. A schematic diagram of the biofilm reactor system used in this study is shown in Figure 1. The system consists of two parts, the tube reactor for growth of microorganisms and the flow channel with three integrated photoacoustic sensor heads for generation and in situ investigation of biofilms. The tube reactor has a length of 1000 mm and an inner diameter of 160 mm. The reactor contained a mixture of microorganisms taken from an aerobic sequencing batch biofilm reactor (13) and fed by 18 L of a nutrient solution consisting of 690 mg L⁻¹ sodium acetate, 60 mg L⁻¹ potassium dihydrogen phosphate, 252 mg L⁻¹ ammonium sulfate, 19 mg L⁻¹ potassium chloride, and 4 mg L⁻¹ yeast extract. The reactor was aerated with compressed air with a volume flow of 1 L min⁻¹. The content of the tube reactor can be mixed by a centrifugal pump (P1) with volume flows in the range of 100 to 300 L h⁻¹.

The flow channel (Figure 2b) has a length of 260 mm and a volume of 100 mL. For investigation of biofilms at different positions, three photoacoustic sensor heads were integrated into the base plate of the channel. To enhance the adhesion of cells on the sensor heads, the surface of the prisms was modified with an aminoalkylsilane: 1 mL of *N*-(2-aminoethyl)(3-aminopropyl)methyldimethoxysilane was dissolved in a mixture of 10 mL of methanol and 10 mL of water. The surfaces of the prisms were treated with this solution for 12 h at room temperature. To generate biofilms on the sensor surfaces, the content of the tube reactor was pumped through the flow channel by a peristaltic pump, P2 (Ecoline VC-280, Ismatec, Wertheim-Mondfeld, Germany). The volume flow can be varied in the range of 25 mL min⁻¹ to 2.5 L min⁻¹ in steps of 25 mL min⁻¹.

Photoacoustic Sensor Heads. The photoacoustic sensor heads consisted of a 25- μ m-thick piezoelectric poly(vinylidene fluoride) (PVDF) film that was coupled to a transparent prism by a conductive epoxy. The piezoelectric detector was circular with a diameter of 5 mm, allowing a representative area of 20 mm². The piezoelectric film was integrated into a BNC socket to eliminate electromagnetic interference. The sample was irradiated through one side and the base of the prism. In this way, an indirect detection scheme as described earlier by Karabutov et al. (14) was realized; i.e., excitation and detection of pressure waves are

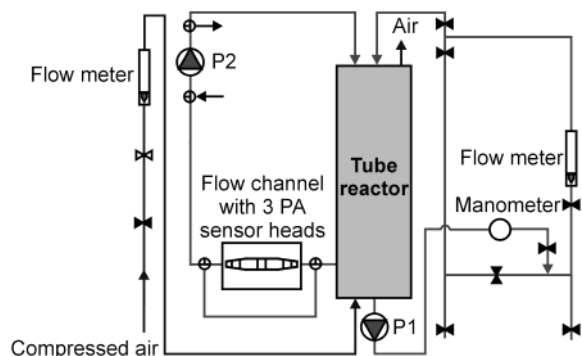


FIGURE 1. Biofilm reactor system (P1, centrifugal pump; P2, peristaltic pump).

performed from the same side of the sample. A detailed description of the sensor head can be found in ref 15.

Photoacoustic Sensor System. The sensor system used in this study is presented in Figure 2a. Throughout all experiments, a Q-switched, frequency-doubled Nd:YAG laser (Surelite 10-I, Continuum, Santa Clara, CA) with a pulse width (fwhm) of 6 ns and a repetition rate of 10 Hz was used for excitation at $\lambda = 532$ nm. The laser beam was attenuated by a beam attenuator (Newport, Irvine, CA), focused by a plano-convex lens ($f = 100$ mm), and coupled into an optical fiber (550- μm diameter, HCG-MO550T-10, Laser Components, Santa Rosa, CA), which guided the laser radiation to the photoacoustic sensor heads.

The photoacoustic signal was fed via a BNC socket into a preamplifier (Femto Messtechnik, Berlin, Germany), and the amplified output signal was recorded by a four-channel digital storage oscilloscope (TDS 540, Tektronix) for a period of 2 μs with a temporal resolution of 2 ns. For improved signal-to-noise ratios, the signal was averaged over 100 laser pulses. The synchronization of the digital storage oscilloscope with the laser pulse was performed with a trigger signal.

All components of the sensor system were controlled by an in-house developed software (LABVIEW 5.1, National Instruments, Austin, TX): flash lamp and shutter of the laser via a serial interface and the digital storage oscilloscope via the IEEE 488 bus. The digital data were transferred to a personal computer through the IEEE 488 bus and stored in three ASCII files, one for each sensor head.

Data Analysis. PAS is based on the absorption of electromagnetic radiation inside a sample and the measurement of nonradiative relaxation by detection of pressure fluctuations. By nonradiative relaxation processes, the absorbed energy is converted into heat. Due to the thermal expansion of the medium, an acoustic wave is generated, which can be detected by pressure-sensitive transducers (16, 17). If a pulsed laser is used for excitation, every laser pulse generates a pressure wave, which can be detected by a piezoelectric transducer directly on the sample surface. The amplitude p of the resulting photoacoustic signal $P(t)$ can be generally described by

$$p \propto (\beta c^2 / C_p) E_0 \mu_a \quad (1)$$

where β is the thermal expansion coefficient, c is the speed of sound, C_p is the heat capacity, E_0 is the pulse energy, and μ_a is the absorption coefficient of the sample (12, 18). The distance between an absorbing object inside a sample and the sample surface can be calculated simply as

$$z = ct \quad (2)$$

where t is the time delay between the laser pulse and the arrival of the acoustic wave at the sample surface. Therefore, time-resolved detection of photoacoustic signals allows depth

profiling of optically or acoustically inhomogeneous samples (19, 20). By eq 2, the time-dependent signal $P(t)$ can be converted into the corresponding depth-dependent signal $P(z)$. The essential parameter of a medium determining the reflection and transmission properties of acoustic waves, is the acoustic impedance Z given by

$$Z = \rho c \quad (3)$$

where ρ is the density of the medium (21). Acoustic impedance mismatches at interfaces inside a sample lead to reflections of acoustic waves. By measuring the time of arrival of an acoustic reflection, the corresponding layer thickness can be calculated.

In the case of optically inhomogeneous samples, the photoacoustic signal profile is a superposition of the profiles of individual layers. Former investigations with nonscattering hydrogel layers showed the possibilities of depth profiling of acoustically homogeneous but optically inhomogeneous samples (22). First experiments with biofilms showed that growth and depth profiling of biofilms can be done by photoacoustic measurements in the visible spectral range (23). As can be seen in eq 1, the amplitude of photoacoustic signals depends on the absorption coefficient, the laser pulse energy, and the physical properties of the sample. For biofilms consisting predominantly of water, the physical properties of water (with $c = 1500$ m s⁻¹) can be assumed. The temperature dependence of C_p , β , and c was corrected by use of literature data (24). The laser pulse energy was measured by a pyroelectric detector (Rj-7100, Laser Precision Corp., Utica, NY), and all measured photoacoustic signals were normalized to the laser pulse energy.

After calibration of the sensor heads using UV-visible spectrometry as reference, the measured photoacoustic amplitudes were converted into the corresponding absorption coefficient. Therefore, most of the photoacoustic signals presented in this paper are in the unit of the absorption coefficient, i.e., cm⁻¹. In this way, differences in sensitivity of the three sensor heads could be compensated. Baseline correction, normalization of temperature and laser pulse energy, and conversion into absorption coefficient were done on-line by the LABVIEW measurement software.

Calibration of the Photoacoustic Sensor Heads. The sensor heads can be calibrated with aqueous solutions of a photochemically and thermally stable dye of known absorption characteristics ($\lambda_{\text{max}} \sim 532$ nm). Here, dye solutions (Javana, K.F.K., Hallendorf, Germany) with the concentrations 1, 2.5, 5, 7.5, 10, 50, 100, 250, 500, and 750 mg L⁻¹ and 1 g L⁻¹ were prepared. The transmittance of the solutions at 532 nm was determined by a UV-visible spectrometer (Beckman, Fullerton, CA), and the absorption coefficient was calculated according to

$$\mu_a = (1/d) \ln(1/T) \quad (4)$$

where d is the path length and T is the transmittance. Concentrations of ≥ 100 mg L⁻¹ were diluted by a factor of 20 before UV-visible measurement, whereas dilution was not necessary for photoacoustic measurements. For calibration, the photoacoustic amplitudes were plotted versus the absorption coefficients.

Calibration with Iron(III) Oxide Particles. To examine the possibilities of detection of iron(III) oxide particles by photoacoustic measurements at 532 nm, a calibration with particle suspensions was performed. Suspensions containing 10, 25, 50, 100, 150, 250, and 500 mg L⁻¹ Fe₂O₃ (iron(III) oxide powder, <5 μm , Aldrich) in water were prepared by suspending the particles and subsequent sonification in an ultrasonic bath. The photoacoustic signal amplitudes of the suspensions were plotted as a function of their concentrations.

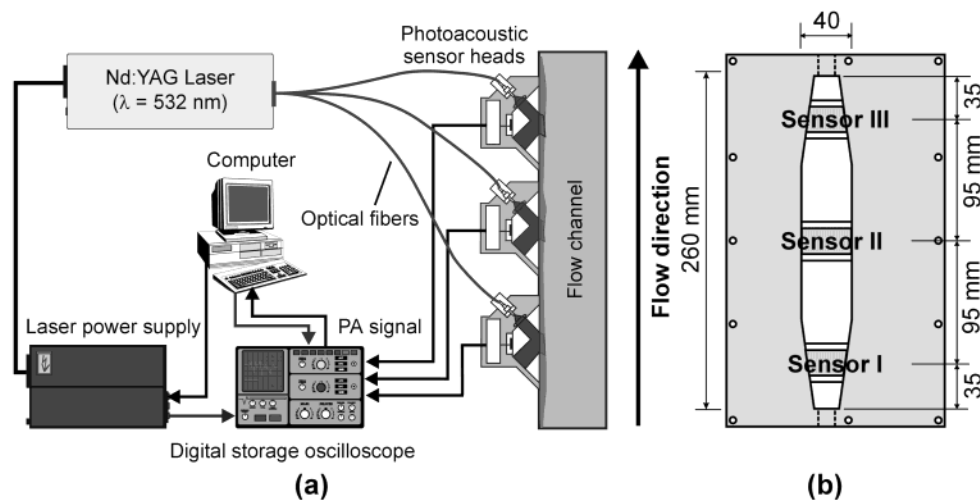


FIGURE 2. Photoacoustic sensor system (a) and flow channel with the three photoacoustic sensor heads (b).

Preparation of Biofilm Models. Agar–agar hydrogels containing iron(III) oxide particles were used as models of biofilms. A suspension of 150 mg L⁻¹ iron(III) oxide in water was prepared as described, 1.5% (w/w) agar–agar (Carl Roth GmbH+Co, Karlsruhe, Germany) was then added, and the mixture was stirred and heated between 80 and 90 °C. The liquid was poured into molds and allowed to cool. In this way, hydrogel layers with a known concentration of Fe₂O₃ particles and a defined thickness of 500 μm and 1 mm, respectively, could be prepared on the surface of a photoacoustic sensor head.

Confocal Laser Scanning Microscopy (CLSM). For validation of the photoacoustic thickness measurement with a real biofilm sample, investigations with an independent microscopic imaging technique were performed. After staining with a fluorescent probe, CLSM allows depth-resolved imaging of biofilms.

A glass slide (76 mm × 26 mm × 1 mm, Marienfeld, Lauda-Königshofen, Germany) was treated with an aminoalkylsilane as described above. The content of the tube reactor consisting of a mixture of microorganisms and a nutrient solution was pumped through the flow channel, and the glass slide was put on the surface of sensor head II inside the flow channel over a time of 10 min.

For photoacoustic measurements, the glass slide was put onto the surface of a sensor head. To improve the transmission of acoustic waves, a small amount of water was poured onto the sensor surface before placing the glass slide. To get homogeneous acoustic properties, water was poured carefully onto the surface of the biofilm. The photoacoustic signal of the slide was recorded four times as described above.

CLSM measurements were performed with a LSM 410 (Carl Zeiss, Jena, Germany) that was coupled with a reverse microscope (Axiovert 135 M, Carl Zeiss). The biofilm sample was stained with a fluorescent probe that is specific for nucleic acids (Syto 17, Molecular Probes, Eugene, OR). In this way, microbial cells were stained. Syto 17 was diluted with PBS buffer (pH 7.4) by a factor of 400. The PBS buffer consisted of 130 mM sodium chloride, 10 mM sodium hydrogen phosphate dihydrate, and 10 mM sodium dihydrogen phosphate dihydrate. Before use, PBS was autoclaved for 21 min at 121 °C. The slide was dipped for 10–15 min into the diluted Syto 17, washed with PBS for 10–15 min at room temperature, and stored in PBS.

Microscopic images of the sample were recorded with the CLSM system using a 10 ×/0.3 NA and a 63 ×/1.3 NA Plan-Neofluar objective, respectively. The data were stored by Carl Zeiss LSM software. While scanning the focus along

the z axis, 2D cut views were recorded and the biofilm thickness was determined at five different positions on the slide.

Repeatability. To examine the repeatability of the formation of biofilms inside the flow channel, the biofilm growth at a volume flow of 300 mL min⁻¹ was monitored for 24 h. After backwashing of the channel for 5 min at 2 L min⁻¹, biofilm growth at 300 mL min⁻¹ was monitored again for 24 h.

Influence of the Flow Conditions. Biofilms were generated inside the flow channel within 2 h as described above. The flow channel was separated from the tube reactor, and 1 L of the nutrient solution was pumped through the flow channel with a volume flow of 250 and 300 mL min⁻¹, respectively. A volume flow of 250 mL min⁻¹ corresponds to flow velocities of 1 cm s⁻¹ at sensor II and 1.4 cm s⁻¹ at the other sensor heads. The flow velocities at 300 mL min⁻¹ are 1.3 and 1.7 cm s⁻¹, respectively. After 24 h, the photoacoustic signal profiles of the biofilms grown at different volume flows were compared.

Change of pH and Biofilm Detachment. The biofilms inside the flow channel were fed for 24 h with 1 L of nutrient solution. Afterward, 7 and 10 mL of sodium hydroxide (1 mol L⁻¹) were added and the pH was changed from pH 8.4 to pH 9.7 and from pH 8.4 to pH 11.1, respectively. Changes in thickness of the attached biomass were monitored by photoacoustic measurements.

Interaction between Iron(III) Oxide Particles and Biofilms. Biofilms were generated inside the flow channel as described above. After 3 days, the flow channel was separated from the tube reactor and the biofilm was fed with 1 L of the nutrient solution described above. After 24 h, a suspension of 125 mg iron(III) oxide particles in 1 L of nutrient solution was pumped through the flow channel with a volume flow of 250 mL min⁻¹. Changes in the optical absorption characteristics of the biofilm were monitored by PAS.

Results and Discussion

Calibration of the Sensor Heads. For determination of the limit of detection (LOD), the photoacoustic signal amplitudes of pure water and five dye solutions in the concentration range of 1–10 mg L⁻¹ was plotted versus the corresponding absorption coefficients determined by UV–visible measurements. The limit of detection was calculated according to the IUPAC 3σ criterion (see Table 1). The LOD for the absorption coefficient is ~0.02 cm⁻¹ for all three sensor heads, which corresponds to a dye concentration of ~1 mg L⁻¹.

TABLE 1. Calibration of the Photoacoustic Sensor Heads with Dye Solutions: Regression Function for the Plot of Signal Amplitudes p versus UV–Visible Absorption Coefficients μ_a , Regression Coefficient (R^2), Number of Samples (n), Number of Repetitions (m), and Limit of Detection (LOD)

sensor head	regression function	R^2	n	m	LOD/ cm^{-1}
I	$p = 20.05 \mu_a - 0.48$	0.9996	7	3	0.027
II	$p = 27.17 \mu_a + 0.51$	0.9996	7	3	0.018
III	$p = 14.50 \mu_a - 1.56$	0.996	7	3	0.020

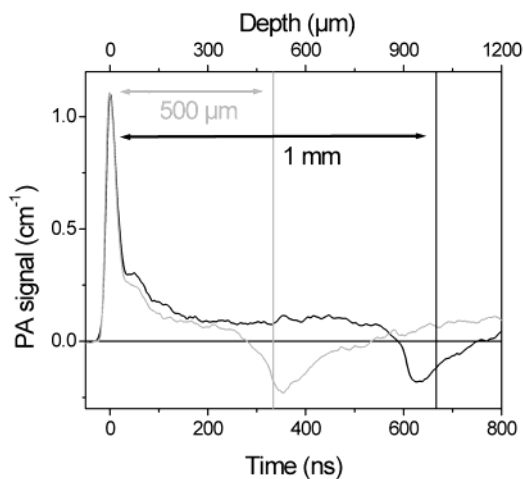


FIGURE 3. Photoacoustic signal profiles of biofilm models consisting of Fe_2O_3 particles enclosed in an agar–agar hydrogel with a thickness of 500 μm (gray) and 1 mm (black).

Table 1 gives the regression function for the calibration with pure water and six dye solutions in the concentration range of 50 mg L^{-1} –1 g L^{-1} . The calibration function was linear from the LOD of 0.02 cm^{-1} up to 23.6 cm^{-1} .

Calibration with Iron(III) Oxide Particles. Suspensions of iron(III) oxide in water were prepared, and the photoacoustic signal amplitude at 532 nm was determined. The photoacoustic signal amplitudes were recorded as a function of the iron(III) oxide concentration. The calibration was linear in the concentration range up to 500 mg L^{-1} . The regression coefficient was 0.997 for the calibration with eight samples and three repeated measurements per sample. The LOD according to the IUPAC 3σ criterion was 4.6 mg L^{-1} .

Photoacoustic Signals of Biofilm Models. An attached biofilm can simply be described by a system consisting of the solid surface (also called the substratum), the biofilm itself, and the bulk liquid phase. This system was simulated with agar–agar hydrogel layers, which presumably have physical properties similar to that of biofilms. In former studies, hydrogels containing a textile dye were used for depth-resolved investigations by PAS (22). With these models, the interface region between biofilm and bulk water cannot be simulated, due to a fast diffusion of the dye inside the hydrogel. In addition, light scattering inside the biofilm cannot be modeled with the simple hydrogel layers.

The problem was solved using agar–agar hydrogels with enclosed iron(III) oxide particles. The layers were prepared as described in the Experimental Section, and water was added to the surface to simulate an aqueous bulk phase. Figure 3 shows the photoacoustic signal profiles of two biofilm models with a thickness of 500 μm and 1 mm, respectively. With a Fe_2O_3 concentration of 150 mg L^{-1} , the absorption coefficient was $\sim 1.1 \text{ cm}^{-1}$, which is in the range of the optical absorbance of real biofilms. According to eq

2, the time scale of the oscilloscope was converted into the corresponding depth scale; the origin of the abscissa at 0 μm corresponds to the surface of the prism. The signal maximum corresponds to the surface of the sensor head. For the whole depth range inside the absorbing and scattering layer, the signal has a positive value. At the interface between hydrogel and water, the signal becomes negative and reaches its minimum.

As exhibited in Figure 3, the biofilm thickness can be derived from the time delay between maximum and minimum of the photoacoustic signal. The minimum of the photoacoustic signal of the 500- and the 1000- μm layer is at 531 and at 940 μm , respectively. The depth resolution of the sensor heads, which was determined in former studies, is $\sim 10 \mu\text{m}$ (22). The deviations obtained in the measurements of the biofilm models are +31 and $-60 \mu\text{m}$ and are therefore larger than the depth resolution. This is obviously due to the uncertainty of the sample preparation, which leads to deviations of 6% in both cases.

The maximum of the signal is not affected by the thickness of the layer, it depends only on the absorption coefficient and the photon density at the sample surface. The photon density is affected by absorption and scattering of light. Due to backscattering, the photon distribution is shifted toward the surface of the sample. The change in photon distribution can change the shape of the photoacoustic signal (25).

As exhibited in eq 1, the amplitude of the photoacoustic signal is a function of the optical absorption coefficient, which depends linearly on the concentration of the absorbing compound. Photoacoustic biofilm measurements in this study are performed at 532 nm. In the visible spectral range, the incident light is absorbed by various pigments inside the cells and the EPS matrix. Therefore, the photoacoustic signal amplitude depends on the density of the immobilized biomass.

By use of particles enclosed in hydrogel, the properties of a biofilm could be modeled: the acoustic properties by agar–agar and the optical properties by Fe_2O_3 particles, which absorb and scatter laser radiation with $\lambda = 532 \text{ nm}$.

Confocal Laser Scanning Microscopy. After the investigations with biofilm models, thickness measurements were validated with real biofilm samples using CLSM as independent microscopic imaging technique. Biofilms were generated on the surface of a glass slide as described in the Experimental Section. The biofilm was investigated by photoacoustic spectroscopy and afterward by CLSM measurements.

Figure 4 exhibits an image of the biofilm that was recorded using a $63\times/1.3 \text{ NA}$ Plan-Neofluar objective. The image is a cut view of a $156.3 \mu\text{m} \times 156.3 \mu\text{m}$ large area at 10 μm above the surface of the glass slide. The sample was stained with the fluorescent probe Syto 17, which is selective for nucleic acids. Therefore, microbial cells were stained, which appear as bright dots. Note that some cell clusters are only faintly stained, possibly as a result of reduced stain penetrability or sorption of the dye to the EPS matrix.

Using a $10\times/0.3 \text{ NA}$ Plan-Neofluar objective, the thickness of the biofilm was determined at five positions on the glass slide. The mean value of the five data points was 67 μm with a standard deviation of 4.5 μm . Figure 5 gives the mean value of four photoacoustic signals of the biofilm sample. For comparison, the result of the CLSM measurement is given. The distance between minimum and maximum of the photoacoustic signal was 63.5 μm with a standard deviation of 3.4 μm . The results of both techniques are in good agreement within the depth resolution of the photoacoustic sensor head of 10 μm .

Biofilm Growth and Repeatability. Figure 6 reveals the photoacoustic signal profiles of a biofilm grown on three sensor heads over 24 h. The increase in signal intensity reflects

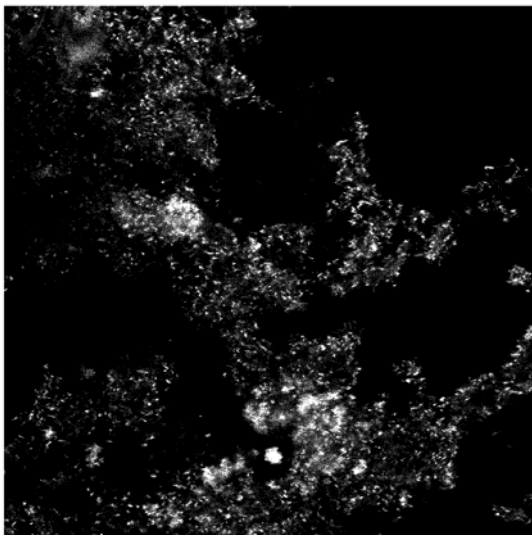


FIGURE 4. Microscopic image of a biofilm on a glass slide determined by confocal laser scanning microscopy using a general nucleic acid stain. The image corresponds to an area of $156.3 \mu\text{m} \times 156.3 \mu\text{m}$ at $10 \mu\text{m}$ above the surface of the slide.

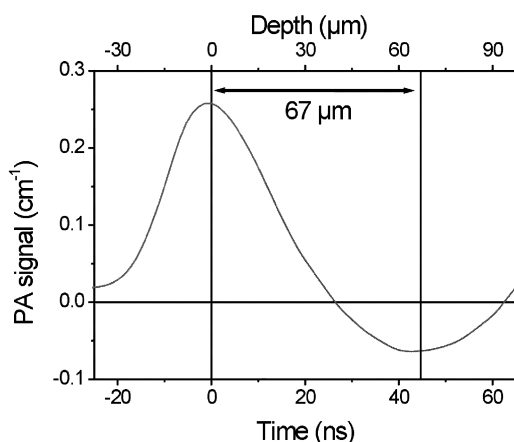


FIGURE 5. Photoacoustic signal profile of a biofilm grown on a glass slide. For comparison, the biofilm thickness determined by CLSM measurements is shown.

the attachment of microbial cells and EPS molecules to the sensor surfaces and the corresponding increase of the density of the immobilized biomass. The amount of the immobilized biomass on the three sensor heads varies simply due to different flow conditions inside the flow channel. At the beginning of the experiment, biofilms with thickness in the range of $40\text{--}60 \mu\text{m}$ were grown. Later, only the flow conditions at sensor heads II and III allowed an increase in biofilm thickness above 1 mm . In most cases, the biofilms on sensor heads II and III had thicknesses in the range of 1 mm or even higher, which is not shown in the diagrams. The biofilm thickness on sensor head I was much lower. The first minimum of the photoacoustic signal profile, which can be identified in the corresponding diagrams, corresponds to the interface between biofilm and bulk water.

After 24 h, the larger part of the biofilms was removed by backwashing the channel and a new growth phase was initiated. The corresponding photoacoustic signal profiles, again after a period of 24 h, are shown in Figure 6. Clearly, signal profiles before and after backwashing are very similar. Even the signal amplitudes 24 h after the second growth phase differ only about $\pm 15\%$ from the first experiment.

Microorganism growth inside the bulk phase during the relatively long experiment time of 48 h had a negligible effect.

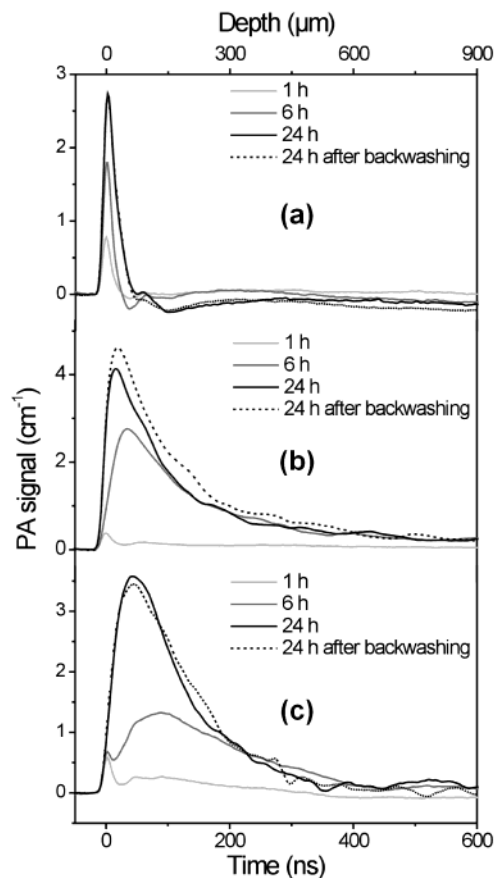


FIGURE 6. Photoacoustic signal profiles of biofilms growing on sensor head I (a), sensor head II (b), and sensor head III (c) before and 24 h after backwashing.

The optical absorption of the biofilm led to an attenuation of the laser pulse, and therefore, the small change in optical absorption of the bulk liquid in the visible range could not be detected.

Influence of the Flow Conditions. Figure 7a shows the photoacoustic signal profiles of biofilms grown on the three sensor heads at a volume flow of 250 mL min^{-1} . The distributions of the biomass on sensor heads II and III are very similar, whereas on sensor head I a thinner biofilm was generated. These structural differences are due to different flow conditions inside the channel as described above. Figure 7b shows the signal profiles of biofilms at a volume flow of 300 mL min^{-1} . Compared to the lower flow velocity, the distribution of the immobilized biomass is shifted toward the sensor surface. Not surprisingly, both the flow conditions and the flow velocity influence structure and thickness of biofilms, significantly.

Change of the pH Value. To investigate the influence of variable pH values on biofilms, different concentrations of sodium hydroxide were added to the nutrient solution, which was pumped through the flow channel. The pH influences electrostatic interactions between EPS molecules and influences therefore the stability of the biofilm. Table 2 exhibits the photoacoustic signal amplitudes of biofilms before and after addition of $7 \text{ mmol L}^{-1} \text{ NaOH}$ and a shift from pH 8.4 to pH 9.7. The amplitude at 0 h corresponds to the biofilm before the alkalinity was increased, and all signal amplitudes in the table are normalized to that value. The change of the pH value to 9.7 does not affect the biofilm; the observed small increase in signal intensity was due to an additional slow growth of the biofilm.

However, as the pH exceeded pH 11, biofilm detachment was observed (see Table 3). The photoacoustic signals of the

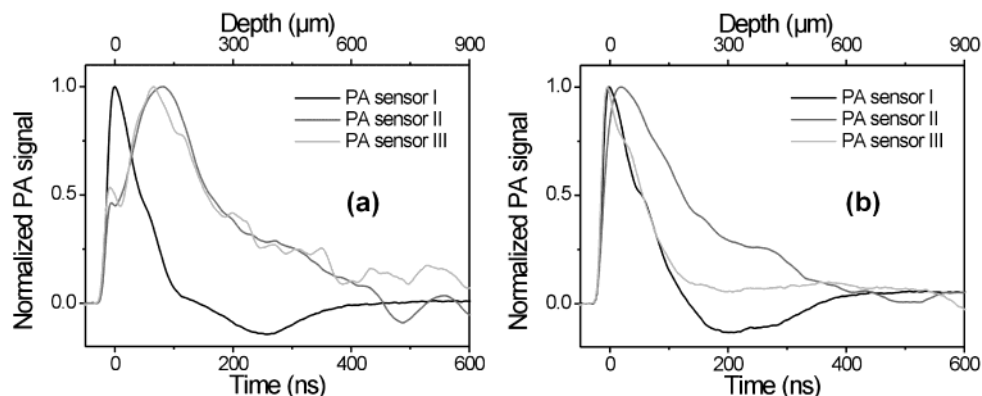


FIGURE 7. Photoacoustic signal profiles of biofilms grown at a volume flow of 250 (a) and 300 mL min⁻¹ (b).

TABLE 2. Change of pH from 8.4 to 9.7 (Volume Flow, 300 mL min⁻¹). Normalized Photoacoustic Signal Amplitudes (ρ_{\max}) and Relative Standard Deviations ($m = 3$)

time/h	PA sensor head I		PA sensor head II		PA sensor head III	
	$\rho_{\max}/\%$	RSD/%	$\rho_{\max}/\%$	RSD/%	$\rho_{\max}/\%$	RSD/%
0	100.0	1.7	100.0	1.3	100.0	2.3
4	100.1	2.1	111.6	5.1	106.7	9.9
20	103.4	3.4	96.8	1.0	115.5	5.5
44	113.7	6.7	111.3	3.2	113.2	6.2

TABLE 3. Change of pH from 8.4 to 11.1 (Volume Flow, 300 mL min⁻¹). Normalized Photoacoustic Signal Amplitudes (ρ_{\max}) and Relative Standard Deviations ($m = 3$)

time/h	PA sensor head I		PA sensor head II		PA sensor head III	
	$\rho_{\max}/\%$	RSD/%	$\rho_{\max}/\%$	RSD/%	$\rho_{\max}/\%$	RSD/%
0	100.0	4.3	100.0	0.5	100.0	3.9
4	86.9	2.0	79.2	0.5	66.6	6.0
20	74.9	2.2	56.5	1.7	25.1	4.2
44	62.6	3.0	4.7	0.5	24.0	0.8

three sensor heads decrease with different rates and reach 62.6% at sensor head I, 4.7% at sensor head II, and 24.0% at sensor head III after 44 h. Different detachment rates are due to different flow conditions and obviously due to structural differences of the biofilms as described above. The mechanism of detachment can be elucidated by comparison of the photoacoustic signal profiles before and after addition of sodium hydroxide (see Figure 8). The decrease in signal intensity is approximately uniform in the whole depth range. Thus, addition of base leads to a continuous detachment which starts at the top layer and subsequently reaches the sensor. Presumably, the biofilm detachment in the alkaline pH range is dominated by sloughing off of small flocs directly from the surface.

The detachment behavior at a volume flow of 250 mL min⁻¹ (see Table 4) is very similar. Biofilm detachment at sensor heads II and III is slightly faster, as at higher volume flows, but the result after 44 h can be compared with the corresponding photoacoustic signal in Table 3. Interestingly, the biofilms on sensor heads II and III having similar structure (see Figure 7a) show similar detachment rates.

Interaction between Iron(III) Oxide Particles and Biofilms. Figure 9a gives the photoacoustic signal profiles of sensor head I before and after addition of a suspension of 125 mg L⁻¹ iron(III) oxide particles in water. Immediately after addition of the Fe₂O₃ suspension ("1 min"), the amplitude increases due to the optical absorption of the Fe₂O₃

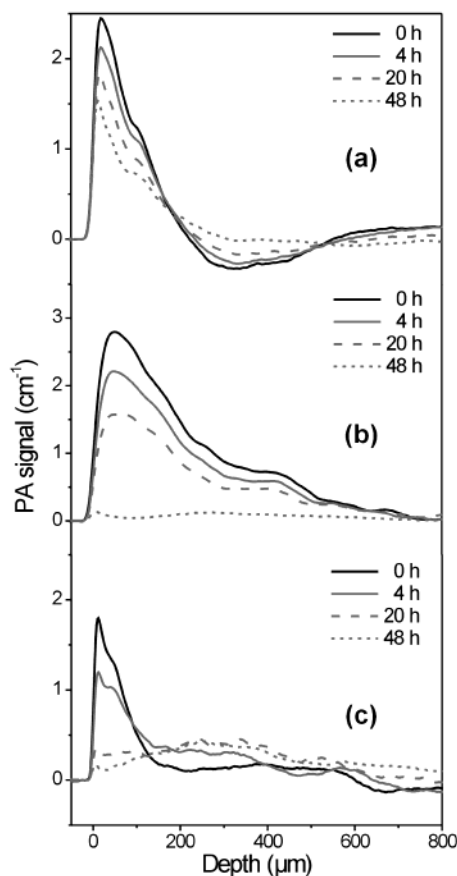


FIGURE 8. Biofilm detachment caused by a change of the pH value from 8.4 to 11.1 (volume flow, 300 mL min⁻¹). Photoacoustic signal profiles of sensor head I (a), sensor head II (b), and sensor head III (c).

suspension. Deposition of Fe₂O₃ particles on the biofilm leads to further increase of the signal amplitude at 6 and 11 min.

The photoacoustic amplitude of sensor head II (see Figure 9b) increases after addition of Fe₂O₃ particles. The increase begins at the sensor surface, i.e., at 0 μ m, and has its maximum at 75 μ m. A measurement after 7 min resulted in a decrease of the amplitude. Obviously, the interaction between particles and biofilm led to a partial detachment of the immobilized biomass. Due to attachment of iron oxide containing biofilm flocs, the signal increased again 17 min after addition of particles.

The increase of the signal at sensor III (see Figure 9c) begins at \sim 30 μ m and has its maximum at 90 μ m. Eight

TABLE 4. Change of pH from 8.4 to 11.1 (volume flow: 250 mL min⁻¹) Normalized Photoacoustic Signal Amplitudes (ρ_{\max}) and Relative Standard Deviations ($m = 3$)

time/h	PA sensor head I		PA sensor head II		PA sensor head III	
	$\rho_{\max}/\%$	RSD/%	$\rho_{\max}/\%$	RSD/%	$\rho_{\max}/\%$	RSD/%
0	100.0	0.7	100.0	1.6	100.0	3.5
4	91.0	4.4	12.7	1.0	15.8	0.6
20	63.6	2.1	5.3	0.2	11.4	0.5
44	49.3	1.4	6.6	0.1	9.9	0.5

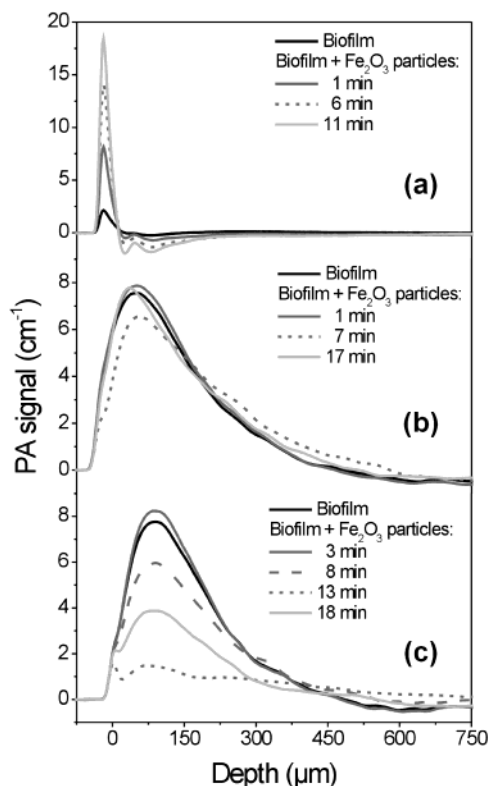


FIGURE 9. Interaction between biofilm and Fe₂O₃ particles. Photoacoustic signal profiles of sensor head I (a), sensor head II (b), and sensor head III (c) before and after addition of particles.

minutes after addition of particles, decrease in signal intensity due to biofilm detachment could be observed. Further biofilm removal occurred beginning at 20 μm , whereas the photoacoustic signal from the sensor surface was approximately constant so that the signal profiles at 13 and 18 min consist of two peaks. Finally, sorption of iron oxide containing flocs led to an increase of the signal amplitude, similar to sensor II.

Thus, biofilm detachment provoked by particles differs from detachment caused by change of the pH value. The

detachment is not uniform for the whole depth range. Detachment happens predominantly in the depth range of $>20 \mu\text{m}$, where the largest part of the particles was sorbed, whereas the base biofilm was not affected by the particles. It should be pointed out again that the depth resolution of the photoacoustic technique is $\sim 10 \mu\text{m}$.

Acknowledgments

The authors acknowledge financial support by Deutsche Forschungsgemeinschaft (DFG) and a grant awarded to T.S. by Max-Buchner-Forschungsstiftung.

Literature Cited

- (1) Wilderer, P. A.; Characklis, W. G. *Structure and Function of Biofilms*; Wiley and Sons: New York, 1989.
- (2) Flemming, H.-C.; Wingender, J. *Water Sci. Technol.* **2001**, *43*, 1–8.
- (3) Frølund, B.; Palmgren, R.; Keiding, K.; Nielsen, P. H. *Water Res.* **1996**, *30*, 1749–1758.
- (4) Jahn, A.; Nielsen, P. H. *Water Sci. Technol.* **1998**, *37*, 17–24.
- (5) Characklis, W. G. In *Biofilms*; Characklis, W. G., Marshall, K. C., Eds.; John Wiley: New York, 1990; pp 55–89.
- (6) Christensen, B. E.; Characklis, W. G. In *Biofilms*; Characklis, W. G., Marshall, K. C., Eds.; John Wiley: New York, 1990; pp 93–130.
- (7) Flemming, H.-C.; Wingender, J.; Moritz, R.; Borchard, W.; Mayer, C. *Spec. Publ.-R. Soc. Chem.* **1999**, *242*, 1–12.
- (8) Headley, J. V.; Gandrass, J.; Kuballa, J.; Peru, K. M.; Yiling, G. *Environ. Sci. Technol.* **1998**, *32*, 3968–3973.
- (9) Mayer, C.; Moritz, R.; Kirschner, C.; Borchard, W.; Maibaum, R.; Wingender, J.; Flemming, H.-C. *Int. J. Biol. Macromol.* **1999**, *26*, 3–16.
- (10) Späth, R.; Flemming, H.-C.; Wuertz, S. *Water Sci. Technol.* **1998**, *37*, 207–210.
- (11) Bott, T. R. *Spec. Publ.-R. Soc. Chem.* **1999**, *242*, 80–92.
- (12) Tam, A. C. *Rev. Mod. Phys.* **1986**, *58*, 381–431.
- (13) Arnz, P.; Arnold, E.; Wilderer, P. A. *Water Sci. Technol.* **2001**, *43*, 167–174.
- (14) Karabutov, A. A.; Podymova, N. B.; Letokhov, V. S. *J. Mod. Opt.* **1995**, *42*, 7–11.
- (15) Kopp, C.; Niessner, R. *Appl. Phys. B* **1999**, *68*, 719–725.
- (16) Rosencwaig, A. *Photoacoustics and Photoacoustic Spectroscopy*; Wiley: New York, 1980.
- (17) Gusev, V. E.; Karabutov, A. A. *Laser Optoacoustics*; AIP Press: New York, 1993.
- (18) Patel, C. K. N.; Tam, A. C. *Rev. Mod. Phys.* **1981**, *53*, 517–550.
- (19) Karabutov, A. A.; Podymova, N. B.; Letokhov, V. S. *Appl. Phys. B* **1996**, *63*, 545–563.
- (20) Oraevsky, A. A.; Jacques, S. L.; Tittel, F. K. *Appl. Opt.* **1997**, *36*, 402–415.
- (21) Trusler, J. P. M. *Physical Acoustics and Metrology of Fluids*; Adam Hilger: New York, 1991.
- (22) Kopp, C.; Niessner, R. *Anal. Chem.* **1999**, *71*, 4663–4668.
- (23) Schmid, T.; Kazarian, L.; Panne, U.; Niessner, R. *Anal. Sci.* **2001**, *17*, 574–577 (Special Issue).
- (24) Weast, R. C. *CRC Handbook of Chemistry and Physics*; CRC Press: Boca Raton, FL, 1983.
- (25) Helander, P.; Lundström, I.; McQueen, D. J. *Appl. Phys.* **1980**, *51*, 3841–3847.

Received for review December 20, 2001. Revised manuscript received July 18, 2002. Accepted July 19, 2002.

ES0158657